Short communication

Diagnostic evaluation of detrimental phenomena in ^{13}C-labeled composite cathodes for Li-ion batteries

Marie Kerlau, Marek Marcinek, Robert Kostecki *

Environmental Energy Technologies Division, Lawrence Berkeley National Laboratory, Berkeley, CA 94720, USA

Available online 30 June 2007

Abstract

^{13}C-carbon black substituted composite $LiNi_{0.8}Co_{0.15}Al_{0.05}O_2$ cathodes were tested in model electrochemical cells to monitor qualitatively and quantitatively carbon additive(s) distribution changes within tested cells and establish possible links with other detrimental phenomena. Raman qualitative and semi-quantitative analysis of ^{13}C in the cell components was carried out to trace the possible carbon rearrangement/movement in the cell. Small amount of cathode carbon additives were found trapped in the separator, at the surface of Li-foil anode, and in the electrolyte. The structure of the carried away carbon particles was highly amorphous unlike the original ^{12}C-graphite and ^{13}C-carbon black additives. The role of the carbon additive, the mechanism of carbon retreat in composite cathodes and its correlation with the increase of the cathode interfacial charge-transfer impedance, which accounts for the observed cell power and capacity loss is investigated and discussed.
© 2007 Published by Elsevier B.V.

Keywords: Li-ion; Cathode; Carbon additives; Raman

1. Introduction

High-power Li-ion cells with graphite anodes and $LiNi_{0.8}Co_{0.2}O_2$ or $LiNi_{0.8}Co_{0.15}Al_{0.05}O_2$ cathodes that were cycled and stored at elevated temperatures display significant impedance rise and capacity fade [1,2]. Impedance measurements of the cell components carried out with a Li–Sn reference electrode indicated that the composite cathode is primarily responsible for the observed cell power loss at elevated temperatures [3,4].

Electrochemical testing of $LiNi_{0.8}Co_{0.15}Al_{0.05}O_2$ cathodes and graphite anodes removed from model pouch-type lithium-ion cells, which were cycled at C/2 over different ranges of DOD and at different temperatures, clearly showed that the cell capacity fade and impedance rise were strongly dependent on temperature, cycling potential limits, and number of charge/discharge cycles [5].

X-ray diffraction spectroscopy measurements failed to detect any noticeable changes in the bulk structure of tested $LiNi_{0.8}Co_{0.2}O_2$ and $LiNi_{0.8}Co_{0.15}Al_{0.05}O_2$ cathodes [1,5]. Possible causes of the increase in cathode impedance and irreversible charge/discharge capacity loss include the forma-

tion of an electronic and/or ionic barrier at the cathode surface [6–8]. This is consistent with our earlier studies [9,10], in which we demonstrated that the non-uniform kinetic behavior of the individual oxide particles was attributed to the degradation of the electronically conducting matrix in the composite cathode upon testing. Carbon additive rearrangement in portions of the tested $LiNi_{0.8}Co_{0.15}Al_{0.05}O_2$ cathodes and/or thin film formation on the surfaces of carbon and oxide particles is closely linked with the observed isolation of oxide active material.

Because the composite cathodes typically consist of an active material, two types of carbon additive, and a binder, suitable instrumental techniques must be applied to obtain lateral resolution comparable to the size and morphology of electrode surface features. *In situ* and *ex situ* application of non-invasive and non-destructive microscopies and spectroscopies, including Raman, fluorescence spectroscopy, SEM, and AFM to characterize physico-chemical properties of the electrode/electrolyte interface at nanometer resolution provide unique insight into the mechanism of specific chemical and electrochemical processes that may be responsible for the electrode and cell degradation. The extraordinary potential of Raman micro-spectroscopy was demonstrated by *in situ* acquisition of space- and time-resolved spectra of positive and carbon negative electrodes in Li-ion cells [4,9,11–14], single oxide or graphite particle in the composite electrode [10,15–17] or single graphite or $LiMn_2O_4$ particle electrodes [18–21].

---

* Corresponding author.
   E-mail address: r_kostecki@lbl.gov (R. Kostecki).

This work presents an example of this methodology used in post-test analysis of interfacial phenomena on the composite $LiNi_{0.8}Co_{0.15}Al_{0.05}O_2$ cathodes. It describes a detailed Raman microscopy study of ^{13}C-carbon black substituted composite $LiNi_{0.8}Co_{0.15}Al_{0.05}O_2$ cathodes which were tested in model electrochemical cells to qualitatively and quantitatively monitor carbon additive(s) distribution changes within tested cells and establish possible links with other detrimental phenomena. The role of the carbon additive in composite cathodes, the mechanism of carbon retreat in composite cathodes and its correlation with the increase of the cathode interfacial charge-transfer impedance, which accounts for the observed cell power and capacity loss, is investigated and discussed.

2. Experimental

Ninety-nine percent pure ^{13}C soft carbon CLM-402 from Cambridge Isotope Laboratories, which emulates physico-chemical properties of acetylene black, was used to manufacture ^{13}C-enriched composite $LiNi_{0.8}Co_{0.15}Al_{0.05}O_2$ cathodes. Prior to the electrode manufacturing the ^{13}C-carbon powder was ball-milled for 6 h to reduce the particle size and obtain powder morphology similar to a standard carbon black additive. The composite electrodes consisted of 84% of $LiNi_{0.8}Co_{0.15}Al_{0.05}O_2$, 4% ^{12}C-graphite, 4% ^{13}C-carbon black, and 4% PVDF binder.

Freshly prepared electrodes were dried in a He-filled glove box antechamber vacuum oven at 120 °C, 42 h. After heat-treatment the electrodes were transferred immediately to a He-filled glove box. All the following tests and measurements were conducted in the same glove box, i.e., the electrodes and cells were never exposed to the air.

Electrochemical cycle life tests were carried out with Swagelok Li-ion cells, which consist of a $LiNi_{0.8}Co_{0.15}Al_{0.05}O_2$ ^{13}C-enriched cathode, Li-metal anode, 1.2 M LiPF$_6$ in ethylene carbonate + diethyl carbonate (EC/DEC, 3:7 vol.) electrolyte, and a Celgard® 2300 separator.

Cycle-life testing was carried out at room temperature and 45 °C at C/10 rate between 3.0 and 4.1 V cell voltage limits. At the end of cycling, the cell was fully discharged at C/25 to 3.0 V (100% DOD), and the discharged cell was disassembled in the glovebox. The cathode was soaked in DEC for 2 h and dried in the glovebox prior to diagnostic evaluations.

A Raman microscope system "Labram" (ISA Groupe Horiba) was used to analyze and map the cathode surface structure and composition. The excitation source was an internal He–Ne (632.8 nm) 10 mW laser. The power of the laser beam was adjusted to 0.1 mW. The diameter of the laser beam at the sample was ~1.2 μm. Individual Raman spectra were processed and deconvoluted using the PeakFit 4.0 commercial software package. SEM imaging was carried out with a Hitachi S-4300 SE/N EDX microscope.

3. Results and discussion

The discharge capacity versus cycle history for the cell tested in this study is shown in Fig. 1. The cycle coulombic efficiency
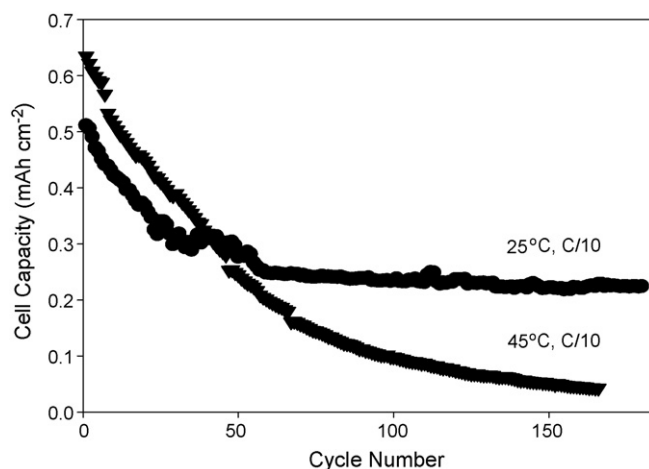

Fig. 1. C/10 discharge capacity of ^{13}C-enriched $LiNi_{0.8}Co_{0.15}Al_{0.05}O_2$/1.2 M LiPF$_6$, EC/DEC/Li-foil Swagelok cells at 25 and 45 °C, 100% DOD.

averaged 99.71%, which led to a 52% capacity fade during C/10 cycling after 180 cycles at room temperature, and 99.47% coulombic efficiency, which corresponds to 91% capacity loss after 170 cycles at 45 °C. The room-temperature cell exhibited most of its discharge capacity loss within the initial 50 cycles whereas the cell tested at 45 °C showed a gradual degradation during cycling. Post-cycling C/25 low-rate capacity measurements showed only 30% and 65% capacity fade at 25 and 45 °C, which indicates that impedance changes in the cell are responsible for a significant fraction of the observed capacity fade at C/10. The observed irreversible discharge capacity loss and impedance rise is entirely attributed to the tested ^{13}C-enriched $LiNi_{0.8}Co_{0.15}Al_{0.05}O_2$ cathode with reference to the fresh cathode. Although it appears that the cathode degradation is the most important contributor to the cell failure mechanism during the long-term cycling versus Li anode, X-ray diffraction spectra of the cycled cathode (not shown here) indicate no new phases or signs of structural damage on the $LiNi_{0.8}Co_{0.15}Al_{0.05}O_2$ active material.

Fig. 2A shows a typical average *ex situ* Raman microscopy spectrum of a fresh ^{13}C-enriched composite $LiNi_{0.8}Co_{0.15}Al_{0.05}O_2$ cathode. It consists of two groups of bands: a broad maximum centered at ~510 cm^{-1}, characteristic for $LiNi_{0.8}Co_{0.15}Al_{0.05}O_2$ oxide, a broad band at ~1280, and two peaks at 1530 and 1582 cm^{-1}. The band at 510 cm^{-1} consists of two Raman-active vibrations characteristic for $LiNi_{0.8}Co_{0.15}Al_{0.05}O_2$ oxide, which crystallizes in the rhombohedral layered structure of α-NaFeO$_2$ (R3m). The bands at higher frequencies originate from carbon black conducting additives, which are the carbonaceous components of the composite cathode (Fig. 2C). The (G) band at 1582 cm^{-1} corresponds to the E$_{2g}$ active mode of ^{12}C-graphite [22]. The low intensity (D) band of ^{12}C-graphite, which is located at ~1324 cm^{-1} is assigned to the A$_{1g}$ mode and is associated with the breakage of symmetry that occurs at the edges of graphite sheets.

The frequencies of vibrational modes of the crystal lattice depend on the interatomic force constants and the atomic masses. Thus, the frequencies of modes can be altered by isotopic sub-
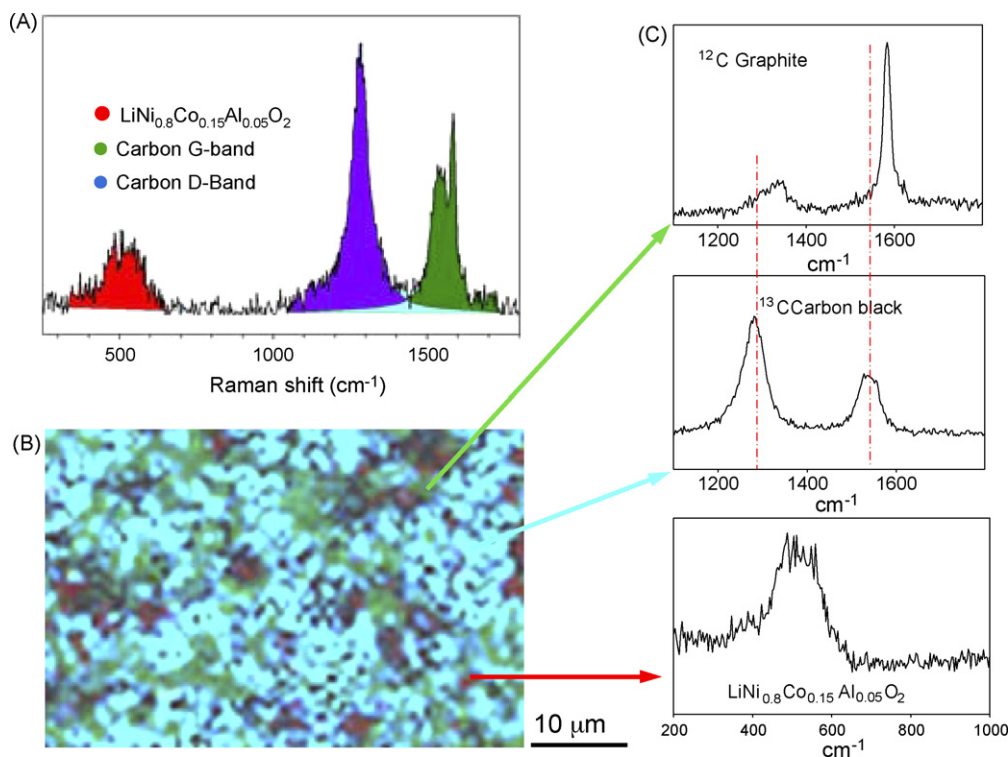
Fig. 2. (A) A typical average Raman spectrum of the fresh ^{13}C-enriched LiNi$_{0.8}$Co$_{0.15}$Al$_{0.05}$O$_2$ electrode, (B) 52 μm × 75 μm Raman microscope image of the fresh ^{13}C-enriched LiNi$_{0.8}$Co$_{0.15}$Al$_{0.05}$O$_2$ cathode, and (C) individual Raman spectra of ^{12}C-graphite, ^{13}C-carbon black, and LiNi$_{0.8}$Co$_{0.15}$Al$_{0.05}$O$_2$. The image was collected at 0.7 μm resolution. The intensities of red, blue, and green colors correspond to the integrated band intensities of the oxide, and D, G carbon bands, respectively.

stitution, and the corresponding band shift can be monitored by Raman spectroscopy. The Raman D and G bands for disordered carbons, where the natural abundance of ^{13}C is 1.1%, are located at ∼1324 and 1590 cm^{-1}, respectively. The change in atomic mass when ^{12}C is replaced by ^{13}C induces a shift and an asymmetric broadening of the Raman lines. The carbon bands' shift that can be calculated from the Redlich-Teller product rule for 100% ^{13}C-substituted carbon black can be expressed by the relation [23]:

$$\hbar\omega_{13C} = 0.9608\hbar\omega_{12C} \qquad (1)$$

where $\hbar\omega_{13C}$ is the position of the Raman lines of ^{13}C-substituted carbon, and $\hbar\omega_{12C}$ is the frequency of bands in ^{12}C-carbons. This gives the band shift for 100% ^{13}C-substituted carbon black of ∼63 and 53 cm^{-1} for G and D bands, respectively. These theoretical values are in agreement with the observed band shift for the ^{13}C-carbon black used in this work.

A semi-quantitative surface analysis of the cathode surface composition was carried out by Raman mapping of a 52 μm × 75 μm section of the cathode surface at 0.7 μm resolution (Fig. 2B). The Raman spectra of individual cathode components recorded at different surface locations are shown in Fig. 2C. The mapping and spectral analysis procedure was described in detail in [14]. Thousands of Raman spectra were deconvoluted, analyzed, and displayed as color-coded points on the composition image map. The color saturations of red, bright blue, which constitutes a superposition of intense blue and green contributions from D and G bands of carbon black, and green

from the dominant G-band in graphite are proportional to the surface concentrations of LiNi$_{0.8}$Co$_{0.15}$Al$_{0.05}$O$_2$, ^{13}C-carbon black, and ^{12}C-graphite, respectively. The resulting color for each location corresponds to the local surface concentration ratio of the components of the composite cathode.

Fig. 3 shows representative micro-Raman surface composition image maps of a ^{13}C-enriched fresh cathode and the cathode from a Li-ion cell that exhibited 52% charge capacity loss. The surface composition Raman maps clearly indicate that the fresh composite electrode is almost fully coated by ^{13}C-carbon black and ^{12}C-graphite. The carbon additives prevent detection of the underlying oxide active material at most locations. Post-mortem micro-Raman analysis of cathodes from the tested cells showed a noticeably higher surface concentration of the active material and lower surface concentration of the carbon additives (Fig. 3B). These results are in concert with our earlier diagnostic Raman observations from commercial Li-ion batteries and model cells which correlated carbon redistribution and the loss of electronic conductance within the composite cathodes [9,10,14].

Carbons display much greater Raman scattering cross-section than LiNi$_{0.8}$Co$_{0.15}$Al$_{0.05}$O$_2$, so the color-coded maps must be considered a semi-quantitative representation of the surface composition. However, they provide clear evidence for a change of surface distribution of the electrode components upon long-term electrochemical charge/discharge cycling.

SEM images (Fig. 4) of the cathodes display large 2–8 μm polycrystalline agglomerates which consist of 100–200 nm pri-
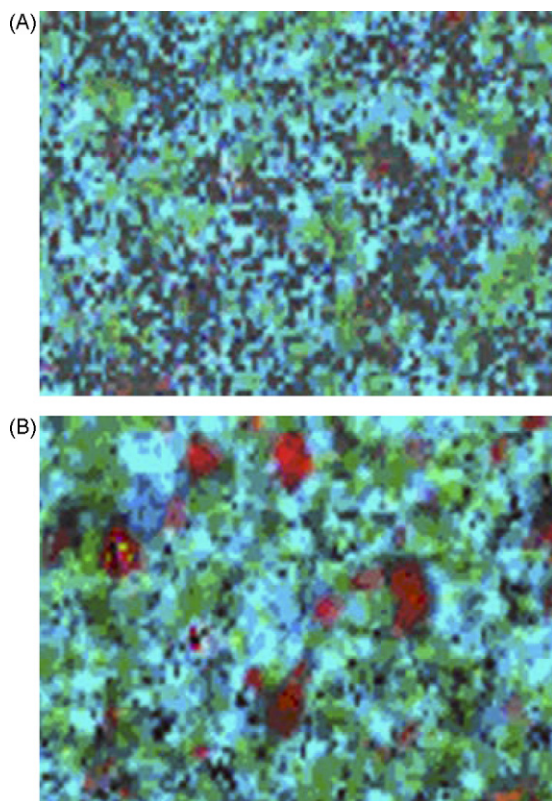
Fig. 3. 52 μm × 75 μm Raman microscope images of the composite ^{13}C-enriched $LiNi_{0.8}Co_{0.15}Al_{0.05}O_2$ cathodes: (A) fresh cathode and (B) cathode from the cycled cell which lost 52% of charge capacity.

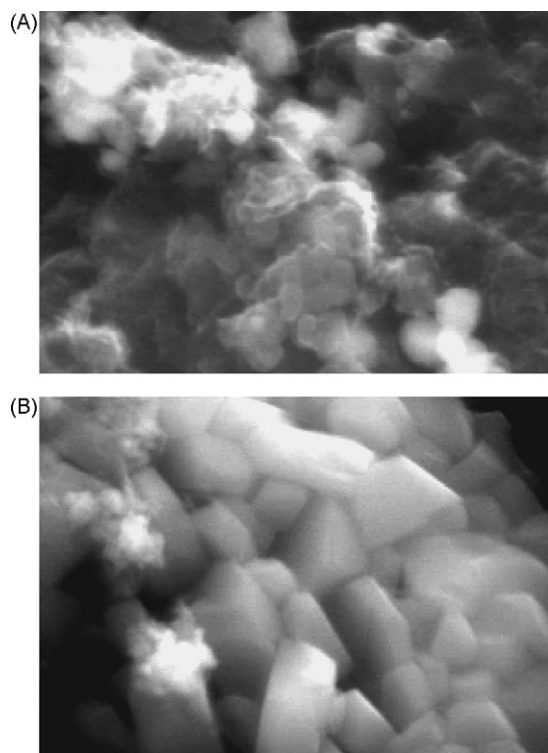mary particles of $LiNi_{0.8}Co_{0.15}Al_{0.05}O_2$. The images show no visible structural damage to the $LiNi_{0.8}Co_{0.15}Al_{0.05}O_2$ oxide particles induced by electrochemical cycling. However, the fresh electrode shows a continuous surface film of ^{13}C-carbon black whereas the agglomerates of the active material appear free of carbon additive in many areas. This result is in agreement with the surface carbon redistribution effect observed on surface composition Raman maps.

A Raman qualitative and semi-quantitative analysis of ^{13}C in the cell components, i.e., the separator, the surface of the anode, and the electrolyte was carried out to trace the possible carbon rearrangement/movement in the cell. Only small and insignificant amounts of fine carbon particles were carried away from the cathode. Micro-Raman spectra of the surface of the Li anode revealed trace amounts of carbon contaminants that could originate from the cathode. We also identified and characterized a modest amount of fine carbon particles trapped in the separator on the anode side (Fig. 5).

Interestingly, almost all micro-Raman spectra collected from the anode and separator reveal contributions from inorganic and organic components of the SEI layer. The peak at $1091\,cm^{-1}$ corresponds to Li_2CO_3 and the broad band at $1450\,cm^{-1}$ as well as peaks that overlap with carbon D and G bands could be consistent with the symmetric vibrations of –C–O and –C=O groups of organic products of the electrolyte decomposition. Micro-Raman spectra of the anode and separator were often hampered by very strong fluorescence signal form fluorophosphate compounds, which originate from the decomposition of $LiPF_6$ [24–26].

Fig. 4. 2.4 μm × 1.7 μm SEM images of the composite ^{13}C-enriched $LiNi_{0.8}Co_{0.15}Al_{0.05}O_2$ cathodes: (A) fresh cathode and (B) cathode from the cycled cell which lost 52% of charge capacity.
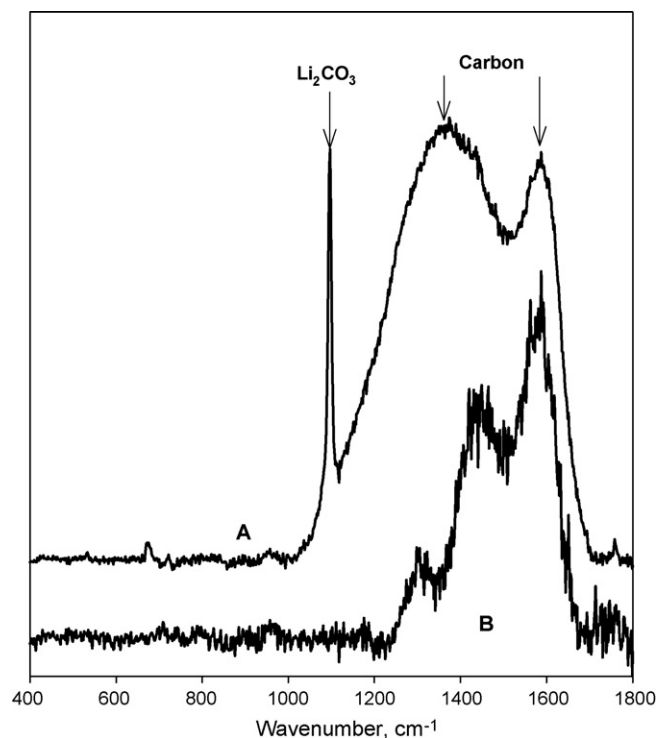

Fig. 5. Micro-Raman spectra of carbon particles found at the surface of the Li anode (A) and trapped in the separator of the cycled cell (B).
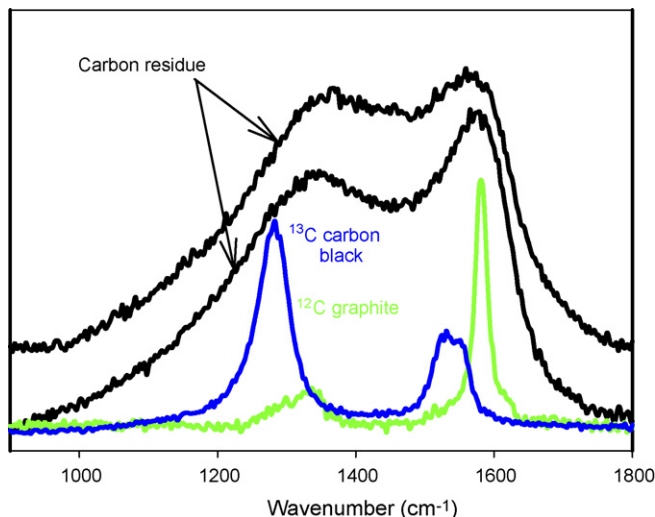
Fig. 6. Two representative micro-Raman spectra of the carbon residue removed from the Li-anode of the cycled cell. The spectra of ^{13}C-carbon black and ^{12}C-graphite additives are provided for reference.

To extract carbon particles from the anode and eliminate possible contributions from the SEI layer's organic and inorganic contaminants, the Li anode was dissolved in distilled water. The remaining black residue was filtered out, dried and analyzed. Fig. 6 shows two representative micro-Raman spectra of the black residue with reference to the spectra of ^{13}C-carbon black and ^{12}C-graphite. Interestingly, the spectra of carbon particles varied slightly at different locations and displayed broad D and G bands typical for highly amorphous carbons unlike the original graphite and ^{13}C-carbon black. On the other hand, contributions from the corresponding ^{13}C- and ^{12}C-carbon D and G bands can be clearly identified.

These amorphous carbons could be natural contaminants of the graphite and ^{13}C-carbon black additives. They also could result from mechanical processing during electrode manufacturing. Another possible mechanism of carbon additive degradation in the cathode is gradual carbon particle delamination due to PF_6^- anion intercalation–deintercalation during electrochemical cycling.

There have been numerous studies of PF_6^- anion intercalation into graphite for potential applications in "dual graphite" cells [27–29]. Discharge capacities of about 100 mA g^{-1} were reported at potentials above 4.2 V. The irreversible losses of capacity observed during charge–discharge cycles prevent any practical application of the graphite cathode in a non-aqueous battery cell. It was suggested that electrolyte decomposition and/or graphite structure destruction by cointercalation of PF_6^- ions and solvent molecules is responsible for the graphite electrode degradation [29]. Unfortunately, no similar studies were carried out on the effects of anion intercalation into amorphous carbons. However, one can assume that carbon blacks could exhibit a similar mode of degradation. Experimental evidence to support this hypothesis will be the subject of a separate study.

Although the amount of carbon additives that could undergo structural damage during mechanical processing and charge–discharge cycling is very small, the consequences for the electrochemical performance of the composite cathode could be severe. Even slight loss and/or rearrangement of carbon additives on the surface of the active material agglomerates can lead to an increased resistance within the agglomerate where primary particles were originally in poor electronic contact with each other. The loss of direct electronic contact between primary particles and the receding carbon matrix leads to partial and, in extreme cases, total isolation of oxide particles. These local effects may be responsible for non-uniform local kinetic behavior of individual oxide particles and the overall degradation of electrochemical performance of the electrode. Thus, the degradation of contact resistances within composite cathodes is likely responsible for the observed cell power and capacity fade.

The experimental evidence presented in this work suggests that carbon particle decrepitation upon anion intercalation/deintercalation followed by removal from the cathode is the likely mode of the composite cathode degradation. However, other detrimental processes such as the loss electrode mechanical integrity, gas evolution, surface film formation, and electrophoretic transport of fine carbon particles across the separator toward the anode can also affect the electrode electrochemical performance. Further fundamental studies of these specific phenomena will be conducted to determine and remedy the critical issues of the materials science and Li-ion battery engineering.

Acknowledgment

References

[1] F Y 2005 Annual Progress Report for Energy Storage Research and Development, http://www1.eere.energy.gov/vehiclesandfuels/pdfs/program/2005_energy_storage.pdf.
[2] X. Zhang, P.N. Ross Jr., R. Kostecki, F. Kong, S. Sloop, J.B. Kerr, K. Striebel, E.J. Cairns, F. McLarnon, J. Electrochem. Soc. 148 (2001) 463.
[3] D.P. Abraham, S.D. Poppen, A.N. Jansen, J. Liu, D.W. Dees, Electrochim. Acta 49 (2004) 4763.
[4] R. Kostecki, F. McLarnon, Electrochem. Solid-State Lett. 5 (2002) A164.
[5] K.A. Striebel, J. Shim, E.J. Cairns, R. Kostecki, Y.-J. Lee, J. Reimer, T.J. Richardson, P.N. Ross, X. Song, G.V. Zhuang, J. Electrochem. Soc. 151 (2004) A857.
[6] D.P. Abraham, R.D. Twesten, M. Balasubramanian, J. Kropf, D. Fischer, J. McBreen, I. Petrov, K. Amine, J. Electrochem. Soc. 150 (2003) A1450.
[7] G.V. Zhuang, G. Chen, J. Shim, X. Song, P.N. Ross, T.J. Richardson, J. Power Sources 4 (2004) 293.
[8] S.W. Song, G.V. Zhuang, P.N. Ross, J. Electrochem. Soc. 151 (2004) A1162.
[9] R. Kostecki, J. Lei, F. McLarnon, J. Shim, K. Striebel, J. Electrochem. Soc. 153 (2006) A669.
[10] J. Lei, F. McLarnon, R. Kostecki, J. Phys. Chem. B. 109 (2) (2005) 952–957.
[11] J.-C. Panitz, P. Novák, J. Power Sources 97/98 (2001) 174.
[12] J.-C. Panitz, P. Novák, O. Haas, Appl. Spectrosc. 55 (2001) 1131.
[13] R. Kostecki, F. McLarnon, J. Power Sources 119–121 (2003) 550.
[14] R. Kostecki, F. McLarnon, Electrochem. Solid-State Lett. 7 (2004) A380.
[15] P. Novák, J.-C. Panitz, F. Joho, M. Lanz, R. Imhof, M. Coluccia, J. Power Sources 90 (2000) 52–58.

[16] D. Ostrovskii, F. Ronci, B. Scrosati, P. Jacobsson, J. Power Sources 94 (2001) 183.

[17] L.J. Hardwick, H. Buqa, Petr Novák, Solid-State Ionics 177 (2006) 2801.

[18] Y. Luo, W.-B. Cai, D.A. Scherson, Electrochem. Solid-State Lett. 4 (2001) A101.

[19] Y. Luo, W.-B. Cai, D.A. Scherson, J. Electrochem. Soc. 149 (2002) A1100.

[20] D.A. Totir, D.A. Scherson, Electrochem. Solid-State Lett. 3 (2000) 263.

[21] K. Dokko, Q. Shi, I.C. Stefan, D.A. Scherson, J. Phys. Chem. B 46 (2003) 12549.

[22] F. Tunistra, J.L. Koenig, J. Chem. Phys. B 53 (1970) 1126.

[23] The original references can be found in K. Nakamoto, Infrared and Raman Spectra of Inorganic and Coordination Compounds, John Wiley & Sons, Inc., 1997.

[24] A. Zaban, D. Aurbach, J. Power Sources 54 (1995) 289.

[25] S.E. Sloop, J.B. Kerr, K. Kinoshita, J. Power Sources 119–121 (2003) 330.

[26] R. Kostecki, L. Norin, X. Song, F. McLarnon, J. Electrochem. Soc. 151 (2004) A522.

[27] J. Besenhard, P. Fritz, J. Electrochem. Soc. 119 (1972) 1697.

[28] A. Jobert, Ph. Touzain, L. Bonnetain, Carbon 19 (1981) 193.

[29] J.A. Seel, J.R. Dahn, J. Electrochem. Soc. 147 (2000) 892.